

GRAVITATIONAL LENS MAGNIFICATION AND THE MASS OF ABELL 1689

A.N. TAYLOR, S. DYE

Department of Astronomy, University of Edinburgh, Blackford Hill, Edinburgh EH9 3HJ, UK; ant@roe.ac.uk, sd@roe.ac.uk

T.J. BROADHURST, N. BENÍTEZ

Department of Astronomy, Campbell Hall, University of California, Berkeley, USA; tjb@wibble.berkeley.edu; benitezn@wibble.berkeley.edu

AND

E. VAN KAMPEN

*Royal Observatory Edinburgh, Blackford Hill, Edinburgh EH9 3HJ,
Theoretical Astrophysics Center, Juliane Maries Vej 30, DK-2100 Copenhagen, Denmark; eelco@tacsg1.tac.dk*

19 June 2018

ABSTRACT

We present the first application of lens magnification to measure the absolute mass of a galaxy cluster; Abell 1689. The absolute mass of a galaxy cluster can be measured by the gravitational lens magnification of a background galaxy population by the cluster gravitational potential. The lensing signal is complicated by the intrinsic variation in number counts due to galaxy clustering and shot-noise, and by additional uncertainties in relating magnification to mass in the strong lensing regime. Clustering and shot-noise can be dealt with using maximum likelihood methods. Local approximations can then be used to estimate the mass from magnification. Alternatively if the lens is axially symmetric we show that the amplification equation can be solved nonlocally for the surface mass density and the tangential shear.

In this paper we present the first maps of the total mass distribution in Abell 1689, measured from the deficit of lensed red galaxies behind the cluster. Although noisier, these reproduce the main features of mass maps made using the shear distortion of background galaxies, but have the correct normalisation, finally breaking the “sheet-mass” degeneracy that has plagued lensing methods based on shear. Averaging over annular bins centered on the peak of the light distribution we derive the cluster mass profile in the inner $4'$ ($0.48h^{-1}\text{Mpc}$). These show a profile with a near isothermal surface mass density $\kappa \approx (0.5 \pm 0.1)(\theta/1')^{-1}$ out to a radius of $2.4'$ ($0.28h^{-1}\text{Mpc}$), followed by a sudden drop into noise. We find that the projected mass interior to $0.24h^{-1}\text{Mpc}$ is $M(< 0.24h^{-1}\text{Mpc}) = (0.50 \pm 0.09) \times 10^{15} h^{-1} \text{M}_{\odot}$.

We compare our results with masses estimated from X-ray temperatures and line-of-sight velocity dispersions, as well as weak shear and lensing arclets. We find that the masses inferred from X-ray, line-of-sight velocity dispersions, arclets and weak shear are all in fair agreement for Abell 1689.

Subject Headings : Cosmology: gravitational lensing, clusters, dark matter

1 INTRODUCTION

The magnitude and distribution of matter in galaxy clusters should in principle provide a strong constraint on cosmological models of structure formation and the mean mass density of the Universe. In addition a direct image of the mass density will tell us much about the relationship between gas, galaxies and dark matter and whether light is indeed a fair – if biased – tracer of mass.

Early techniques for estimating the mass in clusters include dynamical methods, from the line-of-sight velocity dispersion of member galaxies, and X-ray temperature measurements. However these estimates make some strong assumptions about equilibrium conditions in the cluster.

Kaiser and Squires (1993) circumvented this by showing that a more direct method of estimating the mass, with no underlying assumptions about the dynamical or thermodynamical state of the cluster, was to measure the shear field in the source distribution of the cluster background (Kaiser & Squires 1993; Tyson, Valdes & Wenk 1990, Schneider & Seitz 1995). On average the shear pattern of a population of unlensed galaxies should be randomly distributed. But in the presence of a massive gravitational lensing cluster, the shear field is polarized. Since the shear field is related (non-locally) to the surface mass density the shear can be used to estimate the mass distribution – up to an arbitrary constant. The presence of this arbitrary constant, referred to as the “sheet-mass” degeneracy, means that only differen-

tial masses can be measured. Shear maps are conventionally normalised to the edge of the observed field, or such that the inferred mass–density is everywhere positive, and so represent a lower limit on the mass.

Soon after, Broadhurst, Taylor & Peacock (1995; hereafter BTP) showed that the sheet–mass degeneracy could be broken by use of the gravitational lens magnification effect. The number and magnitude–redshift distribution of background galaxies is distorted by the gravitational field of the lensing cluster and in the weak lensing regime this distortion provides a straightforward estimate of the surface mass density. With calibration from off-set fields the cluster mass distribution can be properly normalized.

BTP also suggested that a degraded, but much quicker, estimate of the magnification effect could be made from the distortion of angular number counts of background sources. Broadhurst (1995) found evidence for this distortion in the background counts of the cluster Abell 1689, as did Fort, Mellier & Dantel-Fort (1997) for Cl0024. In this work we apply the methods developed by BTP and extended by Taylor & Dye (1998) to estimate the surface mass density from the distortion of angular counts, including the effects of shot–noise and galaxy clustering, and van Kampen (1998) on estimating the surface mass density in the strong lensing regime, to Abell 1689.

The layout of the paper is as follows. In Section 2 we describe the magnification effect itself. In Section 3 we describe the effects of shot noise and clustering on estimates of the surface mass density. In Section 4 we describe how to estimate the surface mass density in the strong lensing regime using a local approximations, and introduce a new, self-consistent, nonlocal solution for axially symmetric lenses. We apply these methods to map out the mass in the cluster Abell 1689 in Section 5 and find its profile. Our mass estimate is compared to other estimates in Section 6 and our conclusions are presented in Section 7.

2 THE MAGNIFICATION EFFECT

The observed number of galaxies seen in projection on the sky is (BTP, Taylor & Dye 1998)

$$n' = n_0 A^{\beta-1} (1 + \Theta), \quad (1)$$

where n_0 is the expected mean number of galaxies in a given area at a given magnitude. Variations in this mean arise from the angular perturbation in galaxy density, Θ , due to galaxy clustering, and from gravitational lens magnification. The lens amplification factor is

$$A = |(1 - \kappa)^2 - \gamma^2|^{-1} \quad (2)$$

where

$$\kappa = \frac{\Sigma}{\Sigma_{\text{crit}}} \quad (3)$$

is the surface mass density in units of the critical surface mass, Σ_{crit} . The amplitude of the shear field is given by γ and the background galaxy luminosity function is locally approximated by

$$n(L) \sim L^{-\beta}. \quad (4)$$

The amplification index, $\beta - 1$, accounts for the expansion of the background image and for the increase in number as faint sources are lensed above the flux limit.

In the absence of galaxy clustering and finite sampling effects the background galaxy distribution can simply be inverted, via equation (1), to find the amplification. One can then solve equation (2) to find the surface density, with some realistic assumptions about the shear. In Section 4 we discuss various approximations that allow us to do this.

However, given a small resolution scale for the surface amplification, galaxy clustering and finite sampling will in general be an important effect. In the next Section we discuss the effects of intrinsic variation in the distribution of the background galaxy sources.

3 GALAXY CLUSTERING NOISE

The main sources of uncertainty in lens magnification are due to shot-noise, from finite sampling, and the intrinsic clustering of the background source population which introduce correlated fluctuations in the angular counts. As we are viewing small-angles the clustering properties of the background source galaxies are not in general linear, unless the depth of background is sufficient to wash out the clustering pattern. As a result it is not sufficient to make the usual assumption that galaxy clustering can be modelled by a Gaussian distribution.

We can account for the effects of shot-noise and non-linear clustering by modeling the angular counts by a Lognormal–Poisson model (Coles & Jones 1991, BTP, Taylor & Dye 1998) – a random point-process sampling of a lognormal density field. The distribution function of source counts is then

$$P(n) = \frac{1}{n!} \langle \lambda^n e^{-\lambda} \rangle, \quad (5)$$

$$= \frac{\lambda_0^n}{n!} \int_{-\infty}^{\infty} \frac{dx}{\sqrt{2\pi}\sigma} \exp\left(-\frac{x^2}{2\sigma^2} - \lambda_0 e^x - nx\right) \quad (6)$$

where $\lambda = \lambda_0 e^x$ is the local mean density, x is a Gaussian random variable of zero mean and variance σ^2 and $\lambda_0 = n_0 A^{\beta-1} e^{-\sigma^2/2}$ correctly normalises the counts. The linear clustering variance, σ^2 , is related to the nonlinear variance by $\sigma^2 = \ln[1 + \sigma_{\text{nl}}^2]$. We have tested this distribution against available data and find that it is an excellent fit to the distribution of counts in the deep fields. The only parameters are the observed count per pixel, n , and the variance of the lognormal field. The amplitude of clustering of the density field and its dependence of redshift can be estimated from, e.g., the I-band selected galaxies in the Canada–France Redshift Survey in the range $17.5 < I < 22.5$ (Le Fèvre 1996; see section 5.2.3). The quantity required is the variance in a given area of sky, which can be estimated by averaging the observed angular correlation function, $\omega(\theta)$, over a given area:

$$\sigma_{\text{nl}}^2 = \bar{\omega}(\theta) = \frac{1}{\Omega(\theta)} \int_{\Omega} d^2\theta' \omega(\theta'), \quad (7)$$

where $\Omega(\theta)$ is the area.

Our method of approach is then that discussed by BTP. At each pixel in a map of the source counts one uses the distribution equ. (6) as a likelihood function, $\mathcal{L}(A|n, \sigma) =$

$P(n|\sigma, A)$, assuming a uniform prior for the amplification. The surface density is then found from the amplification by making some realistic assumption about the shear and maximizing the likelihood. In the next Section we discuss a number of ways of transforming from the amplification to κ in the strong lensing regime.

4 THE STRONG LENSING REGIME

Transforming from amplification to the surface mass density is potentially non-trivial, as we have no shear information. One could incorporate this from independent measurements of the shear field, but for the present discussion we are interested in developing a completely independent lensing approach. We shall discuss combining shear and magnification elsewhere. In principle one could generate a first guess for the surface mass density and iterate the amplification equation towards a solution of both surface density and shear. However, given the small field of view and uncertainties introduced by parity changes, this can be an unstable problem. In addition, as the solutions are in general multivalued, we would hope to start from as near to the correct solution as possible. In this section we discuss a number of reasonable approximations to solve the amplification equation (2). These can be regarded as solutions in their own right, or as the first best guess to an iterated solution. We begin by discussing the local approximation methods suggested and fully tested on simulated clusters by van Kampen (1998). Then in Section 4.2 we present a new, self-consistent solution to the amplification equation, for κ and γ for an axially symmetric lens.

4.1 Local approximations to the surface mass density

There exist only two local relations between γ and κ that result in a single caustic solution of the amplification equation (2) which is easily invertible (van Kampen 1998): $\gamma = 0$, corresponding to a sheet of matter, and $\gamma = \kappa$, for an isotropic lens. These two relations have corresponding estimators for κ as a function of amplification:

$$\kappa_0 \equiv \kappa(\gamma = 0) = 1 - \mathcal{P}A^{-1/2}, \quad (8)$$

$$\kappa_1 \equiv \kappa(\gamma = \kappa) = \frac{1}{2}(1 - \mathcal{P}A^{-1}), \quad (9)$$

where $\mathcal{P} = \pm 1$ is the image parity.

Let us assume that the surface mass density of the lens is smooth over some scale. In this case, for a sufficiently smooth lens $\gamma \leq \kappa$ (BTP). The equality holds in the case of an isotropic lens, for instance the isothermal lens. The inequality holds for any anisotropic lens, with the sheet mass at the extreme. For a smooth lens these two estimates bound the true value $\kappa_1 \leq \kappa \leq \kappa_0$. Before caustic crossing it can also be shown that $\kappa_1 \leq \kappa_0 \leq \kappa_{\text{weak}}$ holds, where $A = 1 + 2\kappa_{\text{weak}}$ is the weak lensing limit (BTP). Hence the weak lensing approximation will overestimate the cluster mass in the strong regime, usually by a factor of two (van Kampen 1998).

In practice, substructure and asphericity of the cluster will induce extra shear (e.g. Bartelmann, Steinmetz &

Weiss 1995), especially in the surrounding low- κ neighbourhood, where substructure is relatively more dominant and filaments make the cluster most aspherical. This means that the lens will not be smooth for small κ , and therefore κ_1 is a lower limit for the true κ only for the central parts of the cluster, in the case the lens parity is known. Van Kampen (1998) found it to be a good lower limit only for $\kappa > 0.4$ (for the most massive clusters), while for $\kappa < 0.2$, κ_1 is usually fairly close to the true value. For angle-averaged κ -profiles κ_1 is a good lower limit for $\langle \kappa \rangle_\theta > 0.2$. All this has no bearing on κ_0 , which remains a strong upper limit until the first caustic crossing.

An approximation that tries to take these cluster lens features into account, while still giving an invertible $A(\kappa)$ relation, is (van Kampen 1998):

$$\gamma = |1 - c| \sqrt{\frac{\kappa}{c}}, \quad (10)$$

which results in an amplification relation that admits the full four solutions:

$$A^{-1} = |(\kappa - c)(\kappa - 1/c)|, \quad (11)$$

with caustics at $\kappa = c$ and $1/c$. The solution for κ is then

$$\kappa_c = \frac{1}{2c} \left((c^2 + 1) - \mathcal{S} \sqrt{(c^2 + 1)^2 - 4c^2(1 - \mathcal{P}A^{-1})} \right). \quad (12)$$

Solutions are set by choosing the parities $\mathcal{P}, \mathcal{S} = \pm 1$ where \mathcal{P} is the image parity and \mathcal{S} is the sign of $((c^2 + 1)/2c - \kappa)$. Note that the sheet-like solution is recovered by setting $c = 1$.

Figure 1 shows a plot of κ versus the inverse amplification, A^{-1} , for the three estimators. Also shown is the weak field approximation. The points are taken from a simulated lensing cluster (van Kampen & Kargert 1997) which is of comparable size to A1689. It is clear that κ_0 is a strong bound, at least until a caustic is crossed, and that κ_1 provides a very good bound for $\kappa > 0.2$. The weak field approximation however is extremely bad except in the very weak regime ($\kappa < 0.1$). The two-caustic approximation behaves as it is designed to do: a good fit between the other two strong lensing estimators for the central parts of the cluster, while also modelling the $\gamma > \kappa$ behaviour for small κ . These results are fairly robust over a wide range of clusters and for all realistic values of the cosmological density parameter Ω_0 .

4.2 A nonlocal approximation to the surface mass density

An alternative approach is to assume axial symmetry for the lens. Because this fixes a non-local functional relationship between κ and γ (equation 15), we can solve the amplification equation (2) for a self-consistent κ and γ profile. Although we shall apply our results to circularly averaged data, these results hold for any self-similar embedded set of contours.

We define a mean surface density interior to a contour by integration over the interior area, $\Omega(\theta)$,

$$\bar{\kappa}(\theta) = \frac{1}{\Omega(\theta)} \int_{\Omega} d^2\theta' \kappa(\theta') \quad (13)$$

The deflection angle for the axi-symmetric lens is

$$\Delta\theta = \theta\bar{\kappa}, \quad (14)$$

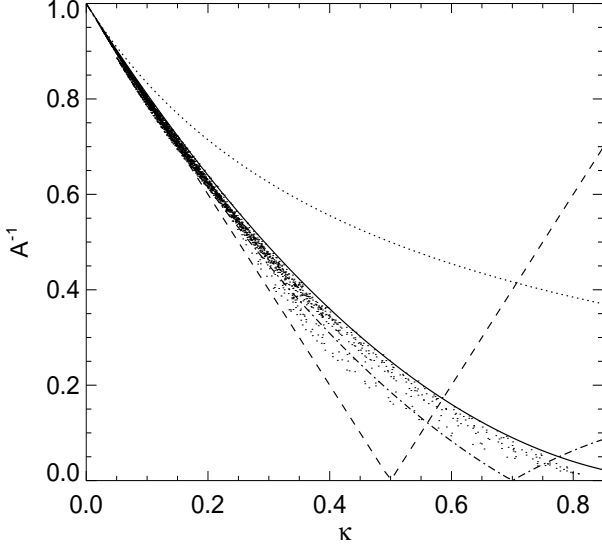


Figure 1. Scatter plot of the surface mass density, κ , versus the inverse amplification, A^{-1} , for a simulated cluster in a CDM universe (see van Kampen 1998 for details). The cluster is at a redshift of 0.183 and the background population at $z = 0.8$. The cluster was selected to look similar to Abell 1689. The solid line is the $\gamma = 0$ strong lensing approximation. Before caustic crossing this is a hard bound on the locus of points. The dashed line is the $\gamma = \kappa$ approximation, which is a good lower bound for $\kappa > 0.2$ for this cluster. The weak-lensing approximation (dotted-line) is seen to be a very bad approximation for $\kappa > 0.1$. The dot-dashed line is a best fit to the simulation for the 2-caustic approximation $\gamma = |1 - c|\sqrt{\kappa/c}$, with $c = 0.7$.

and the shear is given by

$$\gamma = \gamma_t = |\kappa - \bar{\kappa}|. \quad (15)$$

where the tangential term, γ_t , is the only component of shear generated. The amplification factor is given by

$$A^{-1} = |(1 - \bar{\kappa})(1 - 2\kappa + \bar{\kappa})|. \quad (16)$$

One can now simultaneously solve for the surface mass density, shear and amplification by series solution. Firstly we divide the surface mass into consecutive shells with equal separation (any arbitrary separation can be used, we have chosen a regular separation for convenience). If we split $\bar{\kappa}$ into an interior term, η_{n-1} , and a surface term, then for the n^{th} shell we have

$$\bar{\kappa}_n = \eta_{n-1} + \frac{2}{(n+1)}\kappa_n \quad (17)$$

where we have defined

$$\eta_{n-1} = \frac{2}{n(n+1)} \sum_{m=1}^{n-1} m\kappa_m, \quad (18)$$

The surface mass density in the n^{th} shell is then given by

$$\kappa_n = \frac{(n+1)}{4n} \left(n+1 - (n-1)\eta_{n-1} - S[(n-1 - (n+1)\eta_{n-1})^2 + 4n\mathcal{P}A_n^{-1}]^{1/2} \right), \quad (19)$$

where $\mathcal{P}, S = \pm 1$ are again the image parities. The only freedom we have, for a given amplification profile is the choice of the shear on the first shell, $\gamma_1 = \eta_0$, and the parity. It should be noted that given the amplification and having fixed the parities one has to ensure that the first γ satisfies $\gamma^2 \geq \mathcal{P}A^{-1}$, to avoid unphysical solutions. The nonlocal approximation contains both the sheet and isothermal solutions as specific solutions. The uncertainty on κ and γ can be found by simple error propagation of the uncertainty on the measurement of the amplification.

Having shown in Sections 2, 3 and 4 how, in principle, one can measure the surface mass density from angular number counts, in the next section we exploit these methods to measure the mass distribution in the lensing cluster Abell 1689.

5 APPLICATION TO ABELL 1689

In this section we apply the methods discussed in sections 2, 3 and 4 to observational data. We begin by describing the data.

5.1 The Data

5.1.1 Data acquisition and reduction

The data were obtained during a run in February 1994 at ESO's NTT 3.6m telescope, with 10^4 secs integration in the V and I bands, and covers 70 square arcminutes on the cluster. Seeing was similar in both bands, with FWHM of $0.8''$ and a CCD pixel scale of $0.34''$. The EMMI instrument was used throughout. The passbands and exposures were chosen such that the cluster E/S0 galaxies would be bluer than a good fraction of the background, requiring much deeper imaging in the bluer passband for detection. The cluster was observed down to a limiting magnitude of $I = 24$.

The images were debiased and flattened with skyflats using standard IRAF procedures. After this there remained some large scale gradients of a few percent, probably caused by some rotation of the internal lens. We additionally corrected each separate exposure with a smoothed version of itself, obtained after masking out the cluster and other bright objects. Following this we had homogeneous photometry across the field (A further discussion of the reduction procedure can be found in Benítez, et al, 1998, in preparation). The zero point was found to be good to 0.1 magnitudes. High humidity on a few nights meant that some of the data was not photometric, so we calibrated with the photometric data. The object detection and classification was performed with SExtractor.

5.1.2 Separation of cluster and background

To measure the distortion in background counts we must first separate the background from cluster members and mask off the area they obscure. Cluster galaxies were identified from the strong cluster E/SO colour sequence, which forms a horizontal band across the colour-magnitude diagram, shown in figure 2. The sharp upper edge of this band

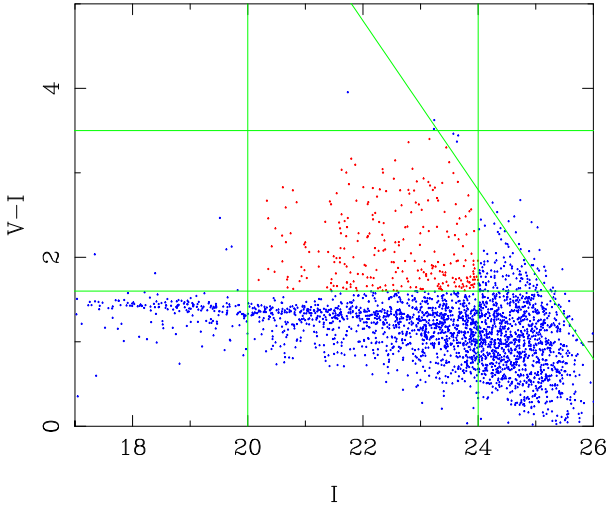


Figure 2. Colour-magnitude diagram for A1689, overlaid with colour cuts used to isolate the cluster members from the background population; $20 < I < 24$, $1.6 < V - I < 3.5$ and $V < 26.8$. The strong horizontal band of galaxies is the cluster E/SO sequence.

represents the reddest galaxies in the cluster. Galaxies redder than this are cosmologically redshifted, and hence represent a background population. As well as isolating cluster members, this selection should also ensure that any foreground galaxies are removed. Anything redder than $V - I = 1.6$ was selected as a background galaxy. Further colour cuts were imposed to ensure completeness of the sample. The range of magnitudes was restricted to $20 < I < 24$ and the V -band limited to $V < 28$. Finally we also cut at $V - I < 3.5$, where the reddest galaxies cut off.

Since the identification of cluster members is important to remove contamination of the background sample we also checked our colour selected candidates with new data from a photometric redshift survey of the same field (Dye et al, 1998, in preparation). We found general agreement with the simpler colour selection.

Having identified foreground and cluster members we produced a mask to eliminate those areas obscured by cluster members that would otherwise bias the mass estimate. To isolate the cluster members for the mask we selected all the galaxies in the colour-magnitude diagram lower than $V - I = 1.6$ and less than $I = 22$. This isolated most of the cluster sequence. The remaining galaxies in the region $V - I < 1.6$ and $I > 22$, $V < 26.8$, we identified as the faint blue background population. It is clear from figure 2 that the distinction between faint cluster member and faint blue background galaxy is rather vague. However, since the faint cluster members are also the smallest, the masked area is fairly insensitive to the exact division. Figure 3 shows the distribution of cluster galaxies and the red background population. The concentric circles are centered on the peak in the cluster light distribution and show the position of the annuli used to calculate the radial profile in section 5.4.

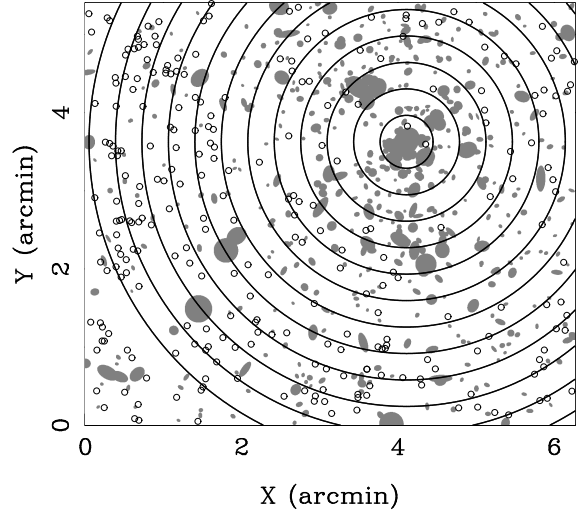


Figure 3. The masked region of A1689. Cluster members were selected using colour information (see text) and then masked over so that these regions do not affect the surface density estimate of background sources. The total region masked is about 10% of the area. The background galaxies are also shown as open circles. Superimposed are the concentric bins used to calculate the radial profile, centered on the peak in the light distribution. North is up and east is to the left.

5.1.3 Selection by colour

Once the cluster galaxies have been isolated, the background galaxies may be sub-divided into a red and blue population, separated by $V - I = 1.6$. The observed slope of the luminosity function for these two populations for $I > 20$ is $\beta_R = 0.38$ and $\beta_B = 1$ (Broadhurst 1995; we shall do a more accurate fit using our colour cuts in section 5.2.2). From equation (1) we expect that the surface density of red galaxies will be suppressed due to the dilation effect, while magnification of the faint blue galaxy population will compensate for the dilation. Hence selecting by colour allows us to identify a population of galaxies with a very flat luminosity function to boost the lensing signal, at the expense of a reduction in galaxy numbers. Simple error analysis shows that the signal-to-noise varies as (Taylor & Dye 1998)

$$S/N = 2|\beta - 1|\kappa A(1 - \kappa + \gamma'/\kappa')\sqrt{n}(1 + n\sigma^2)^{-1/2}, \quad (20)$$

where $' \equiv \partial/\partial R$. While the signal-to-noise is a linear function of the slope of the luminosity function, it only grows with the square-root of the galaxy numbers, assuming Poisson statistics. Hence one can get a better signal-to-noise by pre-selection of the red background population to boost the signal, at the expense of numbers. Equation (20) also shows that one can get a better signal by observing to fainter magnitudes to simultaneously enhance the surface number density and reduce the contribution from intrinsic clustering (see Taylor & Dye, 1998, for a more detailed discussion of observing strategies).

There is also a practical reason for favouring the red galaxy population. While the cluster members are unlikely to be redder than the cluster E/SO sequence the distinction between faint blue galaxies and cluster members, based on selection from the colour-magnitude diagram alone, is

somewhat vague. There may be blue cluster members that will contaminate the sample of blue background galaxies. In the absence of redshift information the blue background population is clearly harder to isolate.

As we have noted the red population has relatively few faint counts, so that the expansion term in equation (1) dominates and there is a net underdensity of red galaxies behind the cluster (see Fig. 4 and Fig. 7). Conversely, faint blue galaxies are numerous and cancel the expansion effect. As expected we found the blue galaxies were uniform across the A1689 field. This is a good indicator that it is the magnification effect at work, and not some spurious contaminant, for example colour gradients across the field, or large scale variations due to clustering. In addition it also indicates that the deficit in the red population is not due to dust obscuration or reddening in the cluster, as this would affect both red and blue populations in equal measure.

5.2 The distribution of background galaxies

In Figure 4 we show the surface distribution of the red population behind A1689, Gaussian smoothed on a scale of $0.35'$. There are 268 background galaxies. The cluster members have been masked out and the masked areas interpolated over. The masked region contributes to only $\approx 10\%$ of the total field. Figure 3 shows the masked region. The cluster center, identified as the peak of the light distribution, is at $(4.1', 3.6')$.

The angular size of the cluster scales like

$$R(\theta) = 0.87 D_A(z_c)(\theta/1')h^{-1}\text{Mpc}, \quad (21)$$

where $D_A(z) = 2(1 - (1+z)^{-1/2})/(1+z)$ is the comoving, dimensionless angular distance in an Einstein–de-Sitter universe. Hence at the redshift of Abell 1689, $z_c = 0.183 \pm 0.001$ (Teague et al 1990), one arcminute is about $0.117h^{-1}\text{Mpc}$.

Figure 4 clearly shows a deficit of galaxies about the central peak in the light distribution at $(4.1', 3.6')$. At $\theta = 0.75'$ there is an arc of very underdense number counts to the South–West of the cluster center, marked by a dashed line (The background is somewhat obscured by the cluster mask to the North–East of the cluster center). This is clear indication of a caustic feature in the background number counts, where the number density drops to zero due to dilation. This exactly corresponds to the radius of the blue arcs observed by Tyson & Fisher (1995) at $\theta = 0.85'$ (see also the radial number counts in section 5.4). This is strong evidence that we have detected the magnification effect in the background counts.

5.2.1 The redshift distribution of background galaxies

The efficiency of lensing varies with the redshift of the background source (BTP). Therefore it is important to estimate the background redshift distribution. Crampton et al (1995) find that Canada–France Redshift Survey (CFRS) has a median redshift of $z = 0.56$ for galaxies in the range $17.5 < I < 22.5$. They also show a colour–redshift diagram that indicates that the red galaxy population ($V - I > 1.6$) has a median redshift of about $z \approx 0.8$ (Crampton et al 1995, their figure 5). More accurately we can integrate the best fit Schechter function found by Lilly et al. (1995)

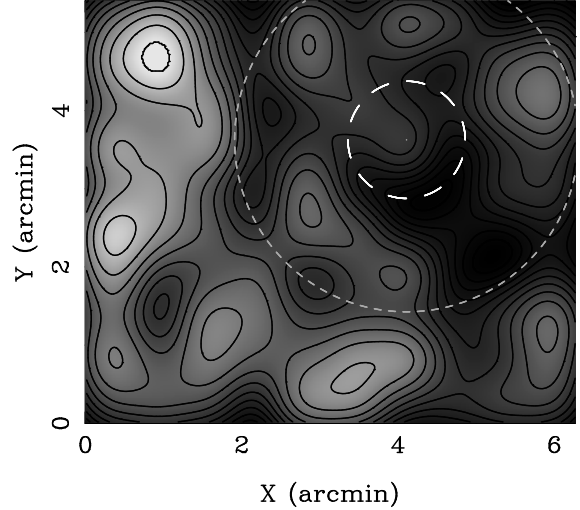


Figure 4. The distribution of red I-band background sources for Abell 1689. Darker grey areas indicate an underdensity of source counts. The image is Gaussian smoothed with a smoothing scale of $0.35'$. The peak of the light distribution is at $(4.1', 3.6')$. The maximum density of objects is 23.0 per square arcminute and the minimum is 1.1 per square arcminute. There are 15 contour lines spaced by $\Delta n = 1.46$ galaxies per square arcminute. A strong caustic feature is seen $0.75'$ from the peak (inner dashed line), more visible to the south–west, as the other side of the peak is masked over. A second feature is found in the radial profile at $2.2'$ (outer dotted line). The image is orientated with East to the left and North to the top.

for the CFRS red galaxy population. This has parameters $\phi^* = 0.0031 \pm 0.00095$, $\alpha = 1.03 \pm 0.15$ and $M^*(B) = -21$, where $M(B) = I - 5 \log_{10}(D_L/10\text{pc}) + 2.5 \log_{10}(1+z) + k$ -correction, where the k-correction is discussed in their paper and $D_L = (1+z)r(z)$ is the luminosity distance. Lilly et al. found no detectable evolution of the luminosity function of the CFRS red population and we assume no evolution. Extrapolating to the magnitude range $20 < I < 24$ we find that the redshift distribution can be well fitted by the function

$$\phi(z) = \frac{\alpha z^2}{z_*^3 \Gamma[3/\alpha]} \exp(-(z/z_*)^\alpha) \quad (22)$$

with $\alpha = 1.8$ and $z_* = 0.78$ to about 5% accuracy over a redshift range of $0.25 < z < 1.5$. The moments of this distribution are

$$\langle z^n \rangle = z_*^n \frac{\Gamma[(3+n)/\alpha]}{\Gamma[3/\alpha]}. \quad (23)$$

Hence for the red galaxy population we find that $\langle z \rangle = 0.96$ and $\sigma_z = 0.42$. To simplify the analysis of the lensing properties of the cluster, we shall assume hereafter that the background distribution is at a single redshift of $z = 0.8$ (the mode of the distribution) and has an uncertainty of $\delta z = 0.4$.

As the caustic indicated by the blue arcs coincides with the magnification caustic, we can presume that the galaxy forming the arcs lies at the same redshift as the magnified red background galaxies, $z \approx 0.8$. At present we do not know the redshift of this arc.

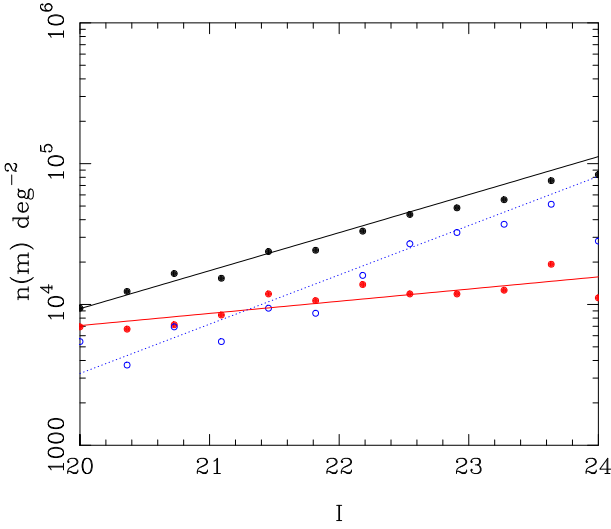


Figure 5. Magnitude distribution of all I-band galaxies (solid dots), the red selected galaxies (grey dots) and the blue background galaxies (open dots). The lines are the best fits to the data.

5.2.2 Number counts of the background galaxy population

Of major importance to the lens magnification method is the normalisation of the background galaxy population. The CFRS is not adequate for this, since their colour cuts were in the rest frame $U - V$, rather than the observed $V - I$. Instead we have used the Keck data of Smail et al (1995), who observed deep VRI images down to a limiting magnitude of $R \approx 27$. The total differential galaxy count rate in the I-band can be approximated by

$$\log_{10} n = (0.271 \pm 0.009)I - 1.45 \quad (24)$$

over the range $20 < I < 24$, where n is per magnitude per square degree. We have applied our colour criteria (see section 5.1) to the Keck data and find that the red galaxy population $V - I > 1.6$, can be well approximated by

$$\log_{10} n(\text{red}) = (0.0864 \pm 0.0187)I + (2.12 \pm 0.41) \quad (25)$$

over the range $20 < I < 24$. Figure 5 shows the magnitude distribution for the full dataset and for the red-selected galaxy population and the best-fit lines. Integrating the fit for the red galaxies yields a total count rate of $n = 12.02 \pm 3.37$ galaxies per square arcminute in the range $20 < I < 24$. Since $\beta = 2.5 d \log_{10} n / dm$, we find that the Keck data implies $\beta_R = 0.216 \pm 0.047$. This is the value of β we shall use in the subsequent analysis.

An alternative, although less exact, method of normalisation is to assume negligible cluster mass at the edge of the field and normalise the cluster to this. In general this would put a lower limit on the mass, and is similar to the method used to normalise shear mass maps. In fact if we do this for A1689 we find a background count rate very similar to that given by the Keck data. The error introduced into the final mass estimate by uncertainties in β scale as $\delta\kappa/\kappa \approx \delta\beta/|1 - \beta|$, which for the Keck data results in a fractional error of around 5%.

We have also fitted the blue counts in the Keck sample (Figure 5). Over the same range as the red counts we find

that $\log_{10} n(\text{blue}) \approx 0.35I - 3.49$, resulting in $\beta_B = 0.88$, close to the lens invariant $\beta = 1$, and a count density between $23 < I < 24$ of $n_0(\text{blue}) = 15.5$ galaxies per square arcminute.

5.2.3 Clustering properties of the background population

The amplitude of clustering of I-band galaxies and its dependence on redshift can be estimated from the CFRS (Le Fèvre et al. 1996). Le Fèvre (1996) find that there is little difference between the clustering properties of red and blue populations of galaxies for $z > 0.5$, implying that the populations were well mixed at this epoch. We therefore apply their clustering results directly to our red galaxy population. They fit their results to a power-law model for the evolving correlation function, $\xi(r) = (r/r_0)^{-\gamma}$, where

$$r_0(z) = r_0(0)(1+z)^{-(3+\varepsilon)/\gamma} \quad (26)$$

where $\varepsilon = 1 \pm 1$ and $r_0(z = 0.53) = 1.33 \pm 0.09 h^{-1} \text{Mpc}$ and $\gamma = 1.64 \pm 0.05$ is in this section the slope of the correlation function.

The quantity we require is the variance in a given area of sky, which can be estimated by averaging the observed angular correlation function, $\omega(\theta)$, over a given area (equation 7). The clustering variance for I-band galaxies then scales roughly like (Taylor & Dye 1998)

$$\sigma_{\text{nl}}^2 = 10^{-2} z^{-2.8} (\theta/1')^{-0.8} \quad (27)$$

where the sampled area is a circle of radius θ and we have assumed unbiased, linear evolution of the density field. The background galaxies are assumed to all lie at $z \approx 1$.

5.3 Reconstructing the surface mass density

In Figure 6 we plot the reconstructed surface mass density of Abell 1689 using the nonlinear local sheet approximation, κ_0 (see section 4.1), changing parity on the caustic line at $\theta = 0.75'$ (see Figure 4). The uncertainty on the peak of the mass distribution is somewhat large (see Section 5.2), but significant features can be seen around the cluster core. There appears to be an extension to the south-west not seen in the cluster galaxy distribution. Interestingly there also appears to be a loosely connected ridge, about $2.4'$ from the peak. We shall discuss this feature further below, but note that the shear mass map derived by Kaiser (1996; figure 2) shows similar extensions and ridge, although the extension to the west is not apparent in the shear map. Two underdense regions are also seen to the south and to the east in both maps. While the comparison is only qualitative and the maps are noisy, we find this very encouraging as these maps are derived from completely independent methods, although the underlying data set is the same.

5.4 The Mass Profile of Abell 1689

While the mass maps are suggestive, a more quantitative measure can be made by angle averaging the counts and calculating the mass profile. Figure 7 shows the radial counts about the peak in the light distribution, normalised to the Keck data. The plotted error bars are only due to Poisson statistics, although in the mass analysis below we shall

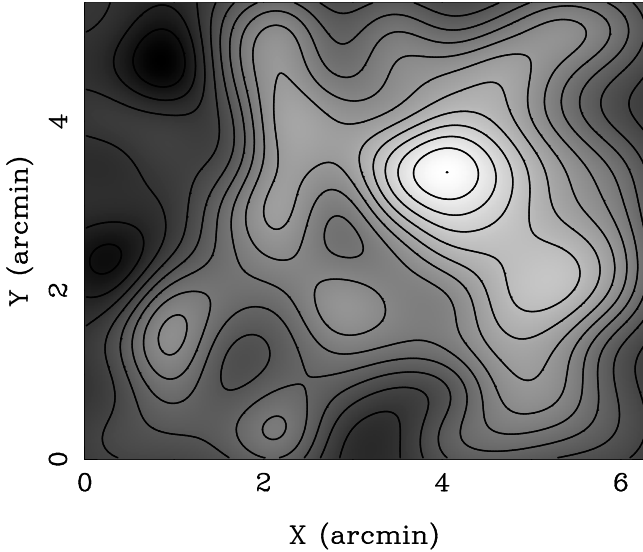


Figure 6. Reconstruction of the surface mass density of Abell 1689 from the red background galaxy population, using the non-linear local sheet approximation and a full likelihood analysis in 2-D. Light regions are high density. Only one caustic line is assumed, at $\theta = 0.75'$ from the peak of the light distribution. The maximum surface density is $\kappa = 1.35$, at $(4.02', 3.41')$, consistent with the peak in the light distribution. The minimum surface mass density is $\kappa = -0.47$. There are 15 linearly spaced contours, separated by $\Delta\kappa = 0.12$ and the map is Gaussian smoothed with a smoothing length of $\theta_S = 0.35'$. North is up and east is to the left.

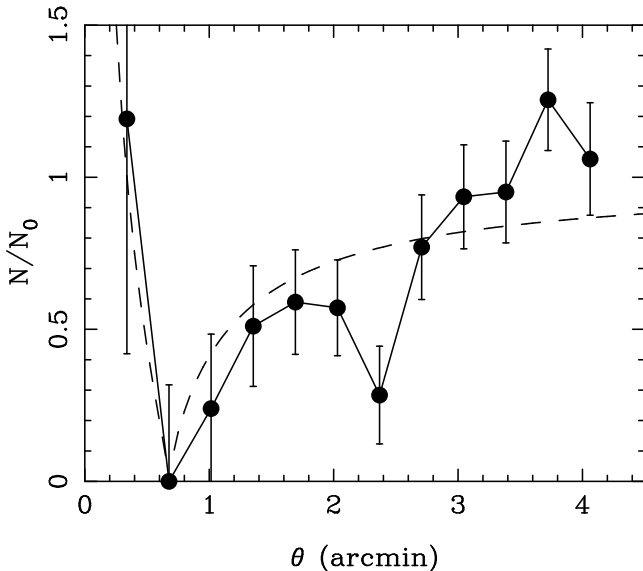


Figure 7. Radial profile of red counts behind Abell 1689. The background count density is $n_0 = 12$ objects/arcmin². Superimposed is the profile for an isothermal model, normalised at the caustic radius, $\theta = 0.75'$ (dashed line).

take into account the effects of clustering. A general trend is clear, and lies close to the prediction for an isothermal lens normalised to the blue arc caustic. This has a surface mass density of $\kappa = 0.375(\theta/1')^{-1}$, corresponding to a virial velocity of 1600 km s^{-1} . Again it is worth emphasizing that the zero of the number counts at $\theta = 0.75'$ corresponds to the caustic inferred from the blue arcs. The second dip will

$r(\text{arcmin})$	N	N/N0	Annulus area	Obscured area
0.33	2	1.19	0.35	0.21
0.67	0	0.00	1.08	0.25
1.01	4	0.24	1.79	0.40
1.35	13	0.51	2.51	0.39
1.69	20	0.59	3.23	0.40
2.03	23	0.57	3.62	0.26
2.36	11	0.28	3.46	0.23
2.70	26	0.77	3.08	0.26
3.04	32	0.94	3.01	0.16
3.38	34	0.95	3.14	0.17
3.72	45	1.25	3.18	0.20
4.06	31	1.06	2.49	0.06

Table 1. Table of angular radius (r in arcminutes), number of red galaxies (N), ratio of galaxies to background (N/N_0), the total area of the annuli (areas are in arcmin²) and area obscured by the mask. The unobscured area is total area – obscured area. The expected number of galaxies in an annuli is $N_0 = n_0 \times \text{unobscured area}$

be discussed in more detail in section 5.4.4. The increase in counts at $\theta = 3.7'$ is likely to be due to a clustering effect.

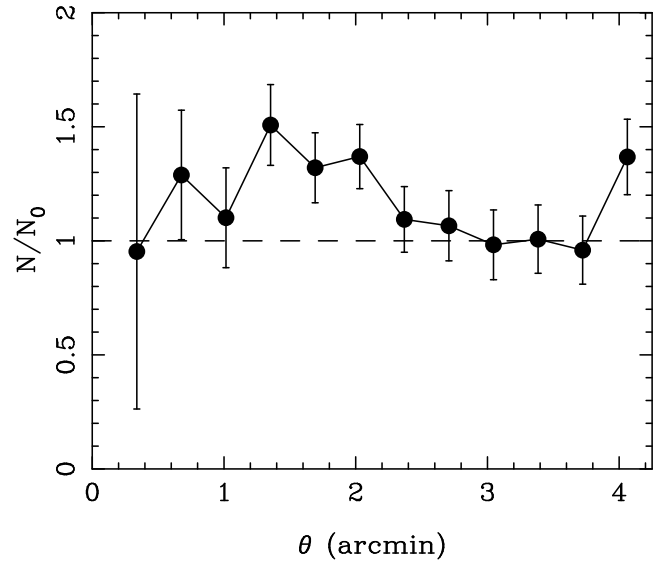


Figure 8. Radial profile of blue counts behind Abell 1689. The background count density is $n_0 = 22$ objects/arcmin². As expected from the nearly lens invariant slope $\beta_{\text{blue}} = 0.88$, the number counts are nearly flat, and at large radii tend towards $n/n_0 = 1$. The slight increase towards the cluster center is probably due to contamination of the counts by blue cluster members

In Figure 8 we show that radial profile for the blue galaxy population, normalised with the Keck data in section 5.2.2. As expected there is no lensing signal. The slight increase towards the cluster center is due to contamination from the blue cluster members.

5.4.1 Local approximations for the surface mass density

Fig. 9 shows the radial mass profile of the cluster Abell 1689 assuming a single caustic at $\theta = 0.75'$. The two solid lines

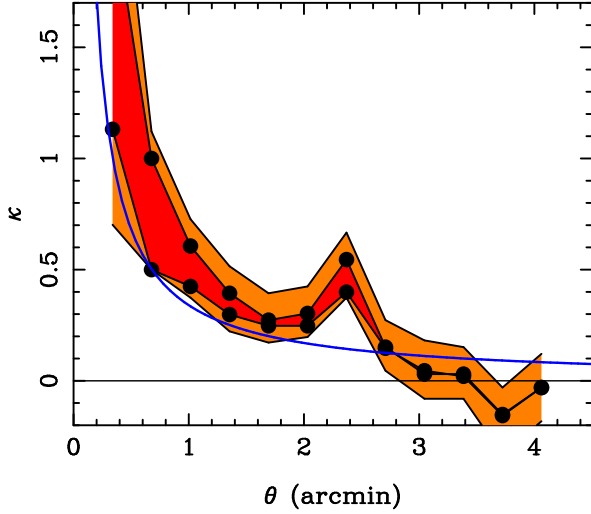


Figure 9. Radial profile of surface mass density of cluster Abell 1689. The dark solid region shows the uncertainty due to the strong lensing estimators. The lighter shaded region is due to the clustering and shot-noise uncertainty of the background population. The solid line is a singular isothermal profile, normalised to the caustic feature at $\theta = 0.75'$.

are calculated using the Lognormal–Poisson likelihood estimator (equation 6) with each of the two strong lensing approximations (equations 9 and 8). The light shaded region indicates the 1σ uncertainty due to both shot noise and the effects of clustering. The dark shaded region indicates the region between the two extreme estimators. Away from the cluster center these agree and are equal to the weak lensing estimator, but noise effects become dominant. Closer to the cluster center the uncertainty due to the shear increases and becomes dominant at $\theta < 1'$. However the cluster mass profile is significantly detected between $1' < \theta < 2.6'$. We also appear to see a deviation from an isothermal profile, which is also plotted. When the procedure was repeated with the center of the annuli offset from the peak of the light distribution the mass profile was weaker and less significant, as one would expect if the peak of the mass density was associated with that of light.

5.4.2 Nonlocal approximation for the mass density and shear

In Figures 10 and 11 we assume axisymmetry and equation (19) to calculate the surface mass-density and shear simultaneously. We set $\gamma_1 = 0.3$ for the first shell. The resulting profile is fairly insensitive to this choice, only affecting the first 2 shells. The uncertainty on the shear in the first shell is small because this must be chosen a priori. However averaging over shells means that the errors do not strongly propagate through to higher radii. Again a mass detection is found between $1'$ and $2.8'$, this time with the shear accounted for. In this region $\kappa \approx 0.4 \pm 0.15$, which is somewhat higher than that found by the shear estimate of $\kappa = 0.2 \pm 0.1$ (Kaiser 1996; note that we quote Kaiser’s colour selected sample, where cluster members that may contaminate the shear estimate have been removed. This corresponds to com-

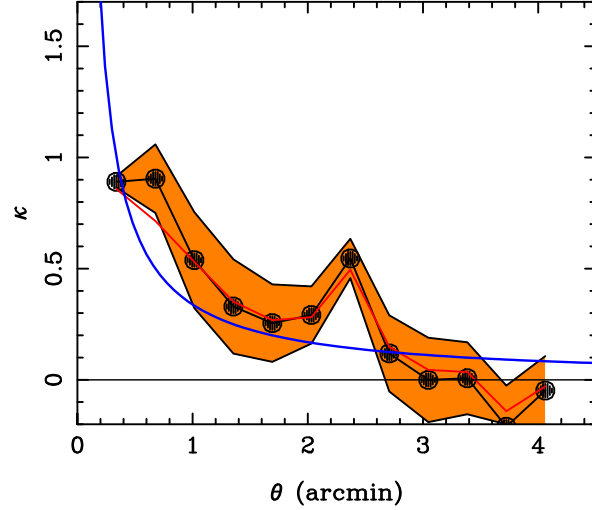


Figure 10. Radial profiles of surface mass density, κ , for A1689 (solid line with dots), calculated by solving the axially symmetric lens equation (19). The shaded regions are 1σ errors calculated via error propagation from the uncertainty on the measured amplification profile. The solid dark line is a singular isothermal profile normalised to the caustic feature at $\theta = 0.75'$. The lighter solid line is the local best fit estimator, κ_c .

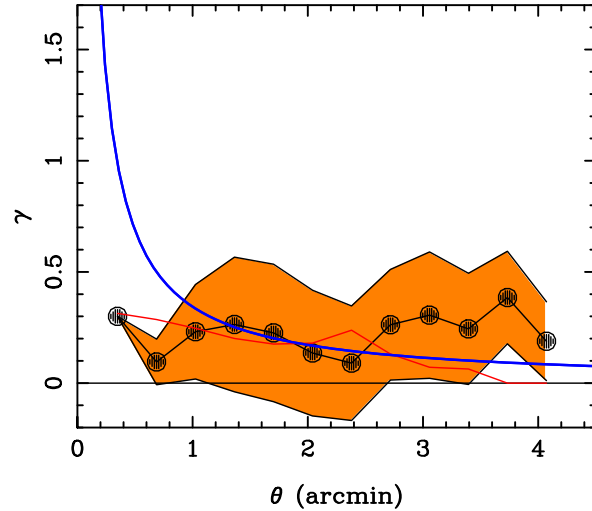


Figure 11. Radial profiles of tangential shear, γ_t , for A1689 (solid line with dots), calculated by solving the axially symmetric lens equation (19). The shaded regions are 1σ errors calculated via error propagation from the uncertainty on the measured amplification profile. The solid dark line is a singular isothermal profile normalised to the caustic feature at $\theta = 0.75'$. The lighter solid line is the local best fit estimator, κ_c .

binning our red and blue background populations. This will change the redshift distribution of the background and include some residual blue cluster contamination which may account for the discrepancy. Also, for the single caustic solution, we see a large spike at $2.2'$, which is not seen in the Kaiser (1996) results. However the shear method correlates points, which may lead to both the suppression of features, and underestimation of the errors.

Our estimate of the shear field is far more uncertain, with $\gamma_t = 0.2 \pm 0.3$ over most of the range. There is a slight increase beyond $2.4'$ due to the spike in the surface mass profile at that radius, but the profile is dominated by noise. This increase is not reflected in the angle averaged measurements of Kaiser (1996), where the mean shear is $\gamma = 0.15 \pm 0.05$.

5.4.3 Local approximation for the surface mass density and shear

Figures 10 and 11 also show κ and γ estimated from the best-fit solution of section 4.1. We find good agreement between the local and nonlocal approximations for κ , but the shear profiles are somewhat different, reflecting that one estimator is local and one nonlocal. However, the large uncertainties produced by each estimator means that we cannot predict the shear profile with much certainty from the available data.

5.4.4 Two background populations ?

An interesting feature of the counts in Figure 7 is the appearance of two pronounced dips, one at $0.75'$ and another one at $2.2'$. While the inner dip has already been identified with a caustic line, the outer dip is somewhat anomalous. A number of possibilities could account for this. The feature was noted in the mass plot as a low signal-to-noise ridge in the density and can be seen in the number counts as a loosely connected ring about the cluster center. One possibility is that this is due to clustering in the background population, combined with a large mass concentration to the south-east of the peak in the light distribution. There are few cluster members in the region of the ridge, or the bump, so the effect is not due to masking.

An alternative is that this is the first glimpse of a second caustic line. In principle a second caustic can be created by placing the background galaxies at two redshifts, one at low redshift, one at high redshift (eg, Fort, Mellier & Dantel-Fort 1996). The observed number counts would then be given by

$$n'/n_0 = A_1^{\beta-1} + \nu(A_2^{\beta-1} - A_1^{\beta-1}) \quad (28)$$

where $A_i = A(f_i)$ with $f_i = \kappa(z_i)/\kappa_\infty = (\sqrt{1+z_i} - \sqrt{1+z_L})/(\sqrt{1+z_i} - 1)$ (BTP), and $i = 1, 2$ for the two galaxy populations. ν is the fraction of galaxies at redshift z_2 . An outer caustic line must be produced by the high redshift population. If we make this population lie at $z = 0.8$, then the low redshift population must lie at $z = 0.3$. Both populations are reflecting the same arc, the difference in projected radii is wholly due to their relative redshifts.

However this would double the predicted mass from lens magnification, making Abell 1689 a very extreme cluster. In addition it seems hard to make a caustic line from the high redshift population for such a massive cluster without

forming a second, inner radial caustic. As the strongest arc is tangential and is seen near the inner arc, one would have to conspire to have a nearby galaxy, at $z = 0.3$, lensed and lying at the same projected radii as the radial arc produced by the high redshift population. This seems highly unlikely.

One could also keep the mass roughly constant and place a second population at $z > 0.8$. This is a possibility, but does not strongly affect our mass estimate assuming a single caustic solution. In the absence of further evidence for a second high redshift population, we shall only consider the single caustic model.

5.5 Mass estimate of Abell 1689

5.5.1 From κ to mass surface density

Assuming that the background galaxies all lie at the same redshift of $z = 0.8$, and given that the surface density scales as

$$\Sigma = \frac{1}{3}\Sigma_0\kappa\frac{(\sqrt{1+z}-1)(1+z_L)^2}{(\sqrt{1+z_L}-1)(\sqrt{1+z}-\sqrt{1+z_L})}, \quad (29)$$

where $\Sigma_0 = 8.32 \times 10^{14} h M_\odot \text{Mpc}^{-2}$ is the mean mass per unit area in the universe, then we find that the surface mass density is

$$\Sigma = 5.9 \times 10^{15} \kappa [h M_\odot \text{Mpc}^{-2}]. \quad (30)$$

Although we have assumed an Einstein-de-Sitter universe, these results only depend weakly on cosmology (BTP).

5.5.2 Uncertainty in the redshift distribution

The error introduced by assuming the background galaxies lie at the same redshift can be estimated by error propagation and assuming $\delta z = 0.4$ (see section 5.2.1). Hence $\delta\Sigma = |\partial\Sigma/\partial z|\delta z$ and the fractional uncertainty on the surface mass density due to the uncertainty in redshift distribution of the background galaxies is $\delta\Sigma/\Sigma = 0.37\delta z = 0.148$. The same error is also found in mass estimates based on the shear pattern.

5.5.3 Uncertainty due to normalisation of background counts

Assuming a sheet mass solution (κ_0 in section 4.1) we find that the uncertainty due to the normalisation of the background counts is $\delta\kappa = (|1-\kappa|/2|\beta-1|)\delta n_0/n_0$. For A1689 and the red galaxy population this is $\delta\kappa = 0.15|1-\kappa|$. For an average $\kappa = 0.5$ the uncertainty is around $\delta\kappa = 0.07$.

5.5.4 The cumulative mass distribution

Figure 12 shows the cumulative mass interior to a shell, calculated from both the nonlocal approximation (section 4.2), and the best-fit local approximation allowing only a single caustic solution (section 4.1). The uncertainties are treated by error propagation. We find that the 2d projected mass interior to $0.24h^{-1}\text{Mpc}$ is

$$M_{2d}(< 0.24h^{-1}\text{Mpc}) = (0.50 \pm 0.09) \times 10^{15} h^{-1} M_\odot, \quad (31)$$

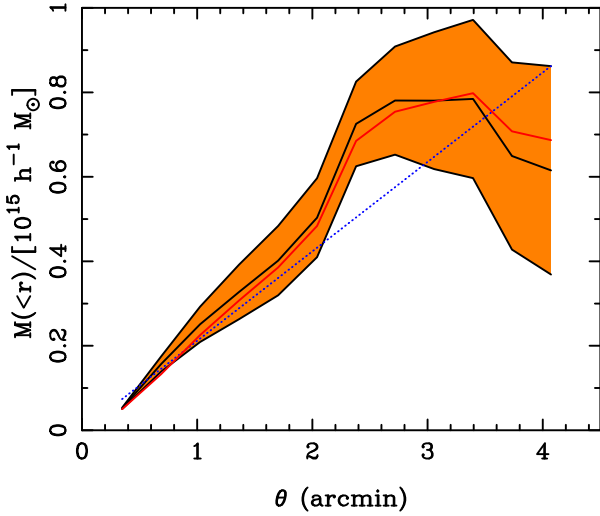


Figure 12. Cumulative mass profile of Abell 1689. The solid dark line and shaded uncertainties are estimated using the axisymmetric nonlocal estimator described in section 4.2. The lighter grey line is the cumulative mass estimated from the best-fit local approximation, κ_c described in section 4.1. Also plotted is the isothermal fit to the blue arc caustic (dotted line), similar to the shear results of Kaiser (1996) and Tyson & Fischer (1995).

and that the two estimators are in good agreement. We find that the projected mass scales like

$$M_{2d}(< R) \approx 3.5 \times 10^{15} (R/h^{-1}\text{Mpc})^{1.3} h^{-1} M_{\odot}, \quad (32)$$

for $R < 0.32h^{-1}\text{Mpc}$, similar to that for an isothermal sphere; $M \sim R$. Hence it appears that A1689 has a near-isothermal core. Beyond $R = 0.32h^{-1}\text{Mpc}$ the lensing signal is lost in background noise, and we can only say that $\kappa \leq 0.1$.

Including the uncertainty from the background redshift distribution and the normalisation of background counts increases the error to about 30%.

6 COMPARISON WITH OTHER MASS ESTIMATES OF A1689 AND INFERRING THE 3D MASS DISTRIBUTION

In this section we compare the mass derived from lens magnification with that found from a number of other, independent measurements. Firstly we compare our results with estimates of the mass based on the shear pattern found around A1689 (section 6.1). The magnification and shear complement each other in that the shear pattern has a higher signal-to-noise, since it is not affected by clustering noise (although with redshift information the magnification can also be measured free from clustering noise – see BTP), but suffers from the “sheet-mass” degeneracy. We shall combine the magnification and shear pattern elsewhere.

While the lens magnification mass is vital for fixing the total 2d projected mass distribution independently of any assumptions about the dynamical state of the cluster, much information can be gained by combining this with other mass estimates, assuming that these are not strongly biased by their reliance on thermodynamical equilibrium. In this section we describe a method for transforming from the

2d lens mass to other cluster characteristics, such as the line-of-sight velocity dispersion (section 6.3) and the X-ray temperature (section 6.4). Discrepancies that arise between these predicted characteristics and the actual measurements can be used to infer information about the mass distribution along the line of sight (Bartelmann & Kolatt, 1997). We find that while there is fair agreement between all of the mass estimates when projection effects are taken into account, the agreement is better if the cluster A1689 is composed of two clusters superimposed along the line of sight and separated by about $\Delta z = 0.02$.

The transformation from a 2-d projected lensing mass to a 3-d mass, line-of-sight velocity dispersion and X-ray temperature can be made using either the isothermal model, or by using relations found in N-body simulations of clusters. While the former provides a simpler method, one has more freedom with simulations to include or exclude the various projection effects that contaminate measurements of these quantities. In this section we shall use the relations found by van Kampen (in preparation) from an ensemble of CDM cluster simulations, all with $\Omega_0 = 1$ and $\sigma_8 = 0.54$. These relations are model dependent, but serve to aid comparison between the various mass measurements. We have also provided a table of quantities (Table 1) where the uncertainties have been calculated by combining the error on the cluster mass with the dispersion found in the deprojection relations.

We begin by comparing the lens magnification mass with the mass determined from the shear field around A1689.

6.1 Comparison with arclets and weak shear

Tyson & Fischer (1995) provide mass profiles of A1689 from arclets, another independent estimator of the mass, normalized to the caustic line indicated by the blue arcs. They find that the 2d projected mass within $R = 0.1h^{-1}\text{Mpc}$ is

$$M_{2d}(< 0.1) = (0.18 \pm 0.01) \times 10^{15} h^{-1} M_{\odot}. \quad (33)$$

They also find that the mass scales like an isothermal sphere out to $0.4h^{-1}\text{Mpc}$, before turning over to an $R^{-1.4}$ profile. This implies that in the regime we probe with the magnification the cumulative mass scales like

$$M(< R) = (1.8 \pm 0.1) \times 10^{15} (R/h^{-1}\text{Mpc}) h^{-1} M_{\odot}. \quad (34)$$

This is very close to the profile we find from lens magnification (equation 32). Using this we scale their results giving

$$M_{2d}(< 0.24) = (0.43 \pm 0.02) \times 10^{15} h^{-1} M_{\odot}, \quad (35)$$

in good agreement with the mass from magnification.

Kaiser (1996) has also calculated κ based on the weak shear method (Kaiser & Squires, 1993), using the same data we have used here for A1689. We noted above that there are qualitative similarities between the weak shear maps and those presented by Kaiser, which is significant since the methods are independent. The mass-density profile found from the shear pattern is also well fitted by an isothermal profile;

$$M_{2d}(< R) = 1.8 \times 10^{15} (R/h^{-1}\text{Mpc}) h^{-1} M_{\odot}, \quad (36)$$

with a 10% statistical uncertainty and further 10% systematic error due to the uncertainty in the redshift distribution

(section 5.5.2). Compared with our 2-d mass Kaiser's analysis suggests that

$$M_{2d}(< 0.28) = (0.43 \pm 0.04) \times 10^{15} h^{-1} M_{\odot}, \quad (37)$$

again in good agreement with that found by the magnification method.

6.2 The 3d mass estimated from lensing alone

The 3-d mass inferred from the 2-d projected mass inside a sphere of radius $r = 0.5h^{-1}$ Mpc is

$$M_{3d}(< 0.5) = (0.72 \pm 0.25) \times 10^{15} h^{-1} M_{\odot}, \quad (38)$$

while the mass inside an Abell radius, $r = 1.5h^{-1}$ Mpc, is

$$M_{3d}(< 1.5) = (1.6 \pm 0.6) \times 10^{15} h^{-1} M_{\odot}. \quad (39)$$

These estimates are probably an overestimate of the true 3d mass since the dispersion in the simulations includes the effect of the alignment of the clusters' principle axis along the line of sight. Given that the inferred 3d mass is so high A1689 is probably lying at the extreme of such a distribution. In such cases the 3d mass may be much lower than mass inferred from a 2d projection. We discuss this possibility in the next few sections.

6.3 Velocity dispersion of Abell 1689

The predicted line-of-sight velocity dispersion estimated from the simulations also includes the effects of superposition of clusters, infall along filaments and interlopers and so predict larger velocities than isolated clusters would. Given this we find that the observed line-of-sight velocity dispersion inferred from the 2d lensing mass is

$$\sigma_v(< 1.5h^{-1} \text{Mpc}) = 3400 \pm 900 \text{ km s}^{-1} \quad (40)$$

for A1689. Again this is very much on the high side for a cluster in a typical CDM universe, and much higher than observational data suggests.

The velocity dispersion measured in a similar manner by Teague et al (1990) is $2355^{+238}_{-183} \text{ km s}^{-1}$, nearly 1σ lower than our estimate. Hence the predicted velocity is not too different from the measured value, so long as both are measured in the same way. The large mass implied by lensing suggests that A1689 is not a single cluster, but a superposition of two smaller clumps. Miralde-Escudé & Babul (1995) have modeled A1689 by two adjacent clumps with velocity dispersions 1450 km s^{-1} and 700 km s^{-1} , suggesting that one clump has a mass 4 times that of the other. Taken together and including the relative velocity of the merging clumps, this accounts for the larger velocities measured earlier. den Hartog & Katgert (1996) have tried to take into account interlopers and find that $v = 1861 \text{ km s}^{-1}$.

If, like Miralde-Escudé & Babul, we assume a double cluster model but place one cluster at $z = 0.18$ with a velocity dispersion of 1500 km s^{-1} and the second at $z = 0.20$ with a velocity dispersion of 750 km s^{-1} , we find that we can reproduce a total projected velocity dispersion of around 2300 km s^{-1} . Figures 4 and 5 of Teague et al (1990) also provide marginal evidence for a second concentration of galaxies at $z = 0.2$. Hence it seems plausible that the high lensing mass of A1689 can be explained by a superposition of clusters.

Quantity	This work	Other
$M_{2d}(< 0.24)$	0.50 ± 0.09	0.43 ± 0.02 (Tyson & Fischer)
		0.43 ± 0.04 (Kaiser)
$M_{3d}(< 0.5)$	0.72 ± 0.25	
M_{500}	1.6 ± 0.65	0.94 ± 0.16 (Yamashita)
$\sigma_v(< 1.5)$	3400 ± 900	2355^{+238}_{-183} (Teague et al)

Table 2. Mass estimates for A1689 based on lens magnification (second column) and from other measurements (third column). Masses are given in units of $10^{15} h^{-1} M_{\odot}$ and velocities are quoted in units of km s^{-1} . Distances are given in $h^{-1} \text{Mpc}$. The other measurements are based on arclets (Tyson & Fischer 1995), the shear pattern (Kaiser 1996), X-ray temperatures (Yamashita 1994) and line-of-sight velocity dispersion (Teague et al 1990). Also given are the 3d mass estimates from lens magnification.

6.4 X-ray mass estimates of Abell 1689

Evrard, Metzler & Navarro (1996) have found that the mass within the radius defined where the mean cluster density is 500 times the critical density is strongly correlated with the cluster temperature. They fit this relation from simulations by

$$M_{500} = 1.11 \times 10^{15} \left(\frac{T_X}{10 \text{ keV}} \right)^{3/2} h^{-1} M_{\odot}, \quad (41)$$

where T_X is the broad-beam temperature and M_{500} is the 3d mass within a radius defined by an overdensity $500\rho_{\text{crit}}$. This radius is roughly given by $r_{500} = 1.175h^{-1} \text{Mpc}$.

X-ray temperatures of A1689 have been measured by both GINGA and ACSA. Yamashita (1994) has analysed this data and finds $T = 9 \pm 1 \text{ keV}$ while Mushotzky and Scharf (1997) find $T = 9.02^{+0.4}_{-0.3} \text{ keV}$. Daines et al (1997) have also recently re-analyzed ROSAT PSPC observations and find a mean temperature of $T_X = 10.2 \pm 4 \text{ keV}$. Note that we are quoting the mean temperature, and incorporated the 40% uncertainty in the error estimate, rather than quoting upper limits as Daines et al do. The major uncertainty in measuring X-ray temperatures here is instrumental, as 10keV is approaching the limit of ROSAT's sensitivity.

Taking the result of Yamashita and the relation found by Evrard et al, we find that

$$M_{500} = (0.95 \pm 0.16) \times 10^{15} h^{-1} M_{\odot}. \quad (42)$$

Using the simulated scaling relations we find

$$M_{500} = (1.6 \pm 0.65) \times 10^{15} h^{-1} M_{\odot} \quad (43)$$

for Abell 1689, implying an X-ray temperature of $T_X = 12.7 \pm 3.4 \text{ keV}$, within the 1σ uncertainty of the measured X-ray temperature. Again, if we consider A1689 as a double cluster, the nearer, larger mass concentration would be detected in X-ray, lowering the expected X-ray temperature. From the velocity dispersions we can infer a temperature nearer to $T_X = 0.7 \text{ keV}$, slightly below, but again in agreement with observations.

In conclusion, although we find a high mass, there is a general consistency between the mass of A1689 estimated from lens magnification and shear. In addition we find a fair agreement between the lens mass and the line of sight

velocity dispersion if we take into account projection effects. Modelling A1689 as a double cluster we find that the velocity dispersion can be much lower, implying two smaller clusters, with the lensing mass a superposition of cluster masses. This hypothesis might also help explain the marginal discrepancy with X-ray temperature.

However, if A1689 is a double cluster, one would expect that the measured velocity dispersion would be higher than that inferred by the lensing mass, due to the cluster separation, while the X-ray mass is lower, since only the more massive cluster dominates the X-ray emission. Our results indicate that Abell 1689 has a larger lensing mass than that implied by both velocity dispersion and X-ray temperature, although given the large uncertainties it is hard to be conclusive.

Finally, A1689 is in projection a highly spherical cluster, in contrast with the majority of clusters which appear extended. While this may be a result of its high mass, it is also possible that A1689 has its major axis aligned along the line of sight, pointing towards a second cluster. While much of the evidence on the mass distribution along the line-of-sight is circumstantial, all of these effects would conspire to give A1689 its impressively massive appearance.

7 DISCUSSION

The absolute surface mass density of a galaxy cluster can be estimated from the magnification effect on a background population of galaxies, breaking the “sheet-mass” degeneracy. To apply this in practice, we have taken into account the nonlinear clustering of the background population and shot-noise, both of which contribute to uncertainties in the lensing signal. A further complication is the contribution of shear to the magnification in the strong lensing regime, where the magnification signal is stronger. We have argued that this can be circumvented by approximate methods that can be either local, where a relationship between surface mass and shear is assumed, or by a nonlocal approximation where only the shape of the cluster is assumed. Both approximations seem to work well on simulated data.

We have applied these methods to the lensing cluster Abell 1689, using Keck data of Smail et al (1995) to normalise the background counts, and the CFRS results to infer the redshift distribution and clustering properties of our data. Using a $\gamma = 0$ approximation of the surface density in the strong lensing regime, we have reconstructed a 2-d mass map for A1689 in the innermost 27 square arcminutes, where a substantial part of the lensing signal comes from. The 2d map has general features similar to those seen from shear maps (Kaiser 1996). This is encouraging for both methods, as they are independent determinations of the mass distribution.

For a more quantitative measure we have binned the data in annuli around the peak in the light distribution and found a significant (5σ) drop in the number counts, dropping to zero where a caustic is inferred from arcs. Local and nonlocal approximations were used to find the κ profile from the number counts, and estimate the shear field. We found these to be quantitatively similar to that found by the shear method.

We have also discussed the possibility of a second pop-

ulation of background galaxies, creating a second dip in the radial number counts and a spike in the mass profile. However we argued that it is unlikely that there is a second low- z population as the cluster mass would be improbably high, and if there is a high- z population it has little effect on our results.

We have calculated a cumulative mass profile for A1689 and find a projected 2-d cumulative mass of

$$M_{2d}(< 0.24h^{-1}\text{Mpc}) = (0.50 \pm 0.09) \times 10^{15} h^{-1} \text{M}_{\odot}. \quad (44)$$

Such a large mass is very rare in a CDM universe normalised to the observed cluster abundance, and may indicate that A1689 is composed of two large masses along the line of sight, and/or filaments connected to the cluster and aligned along the line-of-sight. This is also implied by the high line of sight velocity dispersion which would be enhanced by merging clusters (Miralde-Escudé & Babul 1995) or by infall from aligned filaments.

We have compared our mass estimates with other estimates available in the literature and find that the lens magnification, shear, arclets, line-of-sight velocity dispersions and the X-ray temperature mass estimates are all in reasonable agreement, to within the uncertainties at this time.

The results presented here are from 3 hrs integration on the 3.6m NTT. Longer integration times have the combined benefit of increasing the number of background galaxies, and so reducing shot noise, and of reducing the contribution from cosmic variance (equation 20, Section 5.1.3). Hence by increasing the exposure time we can expect to reduce the uncertainty from lens magnification by a factor of 2 or so.

One drawback of this analysis is the contribution of clustering noise to the background counts. This can be removed using redshift information, either from spectroscopy, or more efficiently using photometric redshift information (BTP). We shall explore this elsewhere (Dye et al, in preparation).

If our results are extended to other clusters we can hope to have a good representation of the total mass distribution, gas and galaxy contents with which to make strong statistical arguments about the matter content of the largest gravitationally collapsed structures in the universe.

Acknowledgments

ANT thanks the PPARC for a research associateship and the University of Berkeley and the Theoretical Astrophysics Center, Copenhagen for their hospitality during the writing of this paper. EvK acknowledges an European Community Research Fellowship as part of the HCM programme and thanks the University of Edinburgh and ROE for their hospitality. This work was supported in part by Danmarks Grundforskningsfond through its funding of the Theoretical Astrophysics Center. SD thanks the PPARC for a studentship. NBL thanks the Spanish MEC for a Ph.D. scholarship, the University of Berkeley for their hospitality and financial support from the Spanish DGES, project PB95-0041. We thank Ian Smail who kindly provided us with a copy of his Keck data. We also thank John Peacock, Alan Heavens, Jens Hjorth, Adrian Webster and an anonymous referee for comments and useful suggestions.

REFERENCES

- Bartelmann M., Steinmetz M., Weiss A., 1995, AA, 297, 1
- Bartelmann M., Kolatt T.S., 1997, MNRAS, submitted, astro-ph/9706184
- Broadhurst T.J., Taylor A.N., Peacock J.A., 1995, ApJ, 438, 49
- Broadhurst T.J., 1995, in AIP Conf. Proc. 336, “*Dark Matter*”, eds S.S. Holt, C.L. Bennett (New York)
- Coles P., Jones B., 1991, MNRAS, 248, 1
- Crampton D., Le Fèvre O., Lilly S.J., Hammer F., 1995, ApJ, 455, 96
- Daines S., Jones C., Forman W., Tyson J.A., 1997, ApJ, submitted
- den Hartog R., Katgert P., 1996, MNRAS, 279, 349
- Evrard et al., 1996, ApJ, 469, 494
- Fort B., Mellier Y., Dantel-Fort M., 1997, AA, 321, 353
- Kaiser N., 1996, in “*Gravitational Dynamics*”, Proc. of the 36th Herstmonceux Conf., eds O. Lahav, E. Terlevich, R.J. Terlevich (Cambridge University Press)
- Kaiser N., Squires G., 1993, ApJ, 404, 441
- Lilly S., Tresse L., Hammer F., Crampton D., Le Fèvre O., 1995, ApJ, 455, 108
- Le Fèvre O., Hudon D., Lilly S.J., Crampton D., Hammer F., Tresse L., 1996, ApJ, 461, 534
- Miralda-Escudé J., Babul A., 1995, ApJ, 449, 18
- Mushotzky R.F., Scharf C.A., 1997, ApJ 482, L13
- Navarro, J.F., Frenk, C.S., White, S.D.M., 1996, ApJ, 462, 563
- Schneider, P. & Seitz, C., 1995, A&A, 294, 411
- Smail I., Hogg D.W., Yan L., Cohen J.G., 1995, ApJLett, 449, L105
- Taylor A.N., Dye S., 1998, submitted MNRAS
- Teague P.F., Carter D., Gray P.M., 1990, ApJSupp, 72, 715
- Tyson J.A., Valdes F., Wenk R.A., 1990, ApJ, 349, L1
- Tyson J.A., Fischer P., 1995, ApJLett, 446, L55
- van Kampen E., 1998, submitted MNRAS
- van Kampen E., Katgert P., 1997, MNRAS, 209, 327
- Yamashita, 1994, in Recontr. de Moriond on “Clusters of Galaxies”, eds F. Durret